Tailoring the framework composition of carbon nitride to improve the catalytic efficiency of the stabilised palladium atoms

Originally published in:
Journal of Materials Chemistry A 5(31), https://doi.org/10.1039/c7ta04607c

Funding acknowledgement:
169679 - Doing more with less: efficient single-atom catalysts based on carbon nitride for sustainable chemical transformations (SNF)

Journal of Material Chemistry: A

ARTICLE

Tailoring the framework composition of carbon nitride to improve the catalytic efficiency of the stabilised palladium atoms

Received 00th January 20xx,
Accepted 00th January 20xx

DOI: 10.1039/x0xx00000x

www.rsc.org/

E. Vorobyeva,[a] Z. Chen,[a] S. Mitchell,[a] R. K. Leary,[b] P. Midgley,[b] J. M. Thomas,[b] R. Hauert,[c] E. Fako,[d] N. López[d] and J. Pérez-Ramírez*[a]

Graphitic carbon nitride (g-C_3N_4) exhibits unique properties for the preparation of single-atom heterogeneous catalysts (SAHCs) due to the presence of sixfold nitrogen-based coordination sites in the lattice. Despite the potential to profoundly affect the metal stabilisation and resulting catalytic properties, no work has previously investigated the effect of modifying the carrier composition. Here, we study the impact of doping carbon in g-C_3N_4 on the interaction with palladium. This is achieved by introducing carbon-rich heterocycles (barbituric acid or 2,4,6-triaminopyrimidine) during the synthesis of bulk and mesoporous g-C_3N_4. Palladium is subsequently introduced *via* microwave-irradiation-assisted deposition, which emerges as a highly effective route for the dispersion of single atoms. Detailed characterisation confirms the controlled variation of the C/N ratio of the lattice and reveals the complex interplay with the crystal size, surface area, amount of defects, basic properties and thermal stability of the carrier. Atomic dispersions of palladium with similar surface densities could be obtained on both the stoichiometric and carbon-doped carriers in mesoporous form, but appreciable differences are observed in the ratio of Pd^{2+}/Pd^{4+}. The latter, which provides a measure of the degree of electron transfer from the metal to the carrier, is found to correlate with the activity in the continuous flow semi-hydrogenation of 2-methyl-3-butyn-2-ol. Density functional theory calculations support the decreased adsorption energy of palladium upon doping with carbon and reveal the potentially significant impact of oxygen-containing defects. The findings demonstrate the importance of understanding the metal-carrier interaction to optimise the catalytic efficiency of SAHCs.

Introduction

Catalytic processes remain heavily reliant on precious metals due to their unparalleled active, selective and stable character. The development of catalysts based on single atoms is of great interest for the efficient utilisation of these metals.[1-5] Compared to state-of-the-art nanoparticle-based catalysts, which only expose a small fraction of surface atoms that can contribute to the activity, achieving a metal dispersion (defined as the number of surface atoms/total number of atoms) of unity is critical to maximise the catalytic efficiency per atom and reduce the amount of metal required. Enhanced performance has been observed over single-atom heterogeneous catalysts (SAHCs) in several relevant processes including hydrogenation,[4] oxidation[6] and water-gas-shift reactions.[7,8] However, the fabrication of SAHCs is a major challenge because of the tendency of atoms to aggregate into clusters and nanoparticles.[9,10] For this reason, the use of a carrier which provides abundant well defined anchoring sites that can strongly bind metal atoms plays a crucial role in their stabilisation.[11-14]

One material that exhibits a highly attractive set of features as a sustainable carrier is graphitic carbon nitride (g-C_3N_4), which can robustly coordinate metal species within sixfold coordination sites in the lattice.[15] The presence of these small, nitrogen-rich crystallographic interstices provides a stability unmatched by the broad related family of N-doped carbons. As well as having demonstrated scalability and being composed of inexpensive, nontoxic, and earth-abundant elements, g-C_3N_4 possesses high chemical and thermal stability and can be prepared with flexible morphology and surface area. Besides, the composition can be easily tuned by using other heteroatom sources.[16] Various metals, including Pd, Pt, Ir and Ag, have been successfully stabilised as single atoms on this carrier.[17] The catalytic superiority of Pd/g-C_3N_4 SAHCs has

[a] Institute for Chemical and Bioengineering, Department of Chemistry and Applied Biosciences, ETH Zurich, Vladimir-Prelog-Weg 1, 8093 Zurich, Switzerland. E-mail: jpr@chem.ethz.ch
[b] Department of Materials Science and Metallurgy, University of Cambridge, 27 Charles Babbage Road, Cambridge, CB3 0FS, United Kingdom.
[c] EMPA, Swiss Federal Laboratories for Materials Science and Technology, Uberlandstrasse 129, CH-8600 Dubendorf, Switzerland.
[d] Institute of Chemical Research of Catalonia (ICIQ) and The Barcelona Institute of Science and Technology, Av. Països Catalans 16, 43007 Tarragona, Spain.

Electronic Supplementary Information (ESI) available: Additional characterisation of the carriers and Pd-containing catalysts including chemical composition, XRD patterns, N_2 isotherms, TGA profiles, further microscopy images, Pd 3*d* XPS spectra, ^{13}C CP-MAS NMR spectra, DRIFT spectra, CO_2-TPD, EXD mapping, DFT and additional catalytic data. See DOI: 10.1039/x0xx00000x

been evidenced in selective hydrogenation reactions, central to the production of many fine chemical and pharmaceutical intermediates, offering an ecological alternative to classical Lindlar-like catalysts that contain high amounts of precious metals and require the use of harmful additives as lead.[18] Atomically-dispersed silver on g-C_3N_4 also out-performed the other Ag-based selective hydrogenation catalysts,[19] while single atom platinum catalysts exhibited remarkable photocatalytic hydrogen evolution activity.[20]

Analogous to the effects widely discussed for catalysts based on deposited metal nanoparticles,[21-23] the interaction with the carrier determines the stability and further impacts the electronic properties of metal atoms.[22,23] However, only very few attempts have been made to modify the carrier structure and correlate the impact on the metal binding strength and performance of SAHCs.[24-26] The effect of the carriers on the electronic properties of the SAHCs is difficult to assess. Experimentally, this is most commonly probed by X-ray photoelectron spectroscopy, fitting the observed signals to species with different oxidation states assuming that the shifts are only related to charge-transfer effects. However, other factors can also affect the peak position including the reduction of the coordination number (from a bulk material to a single atom) and the extent of covalency, and the presence of electric fields. In turn, theoretical models typically compute charges through a Bader-type analysis[27] and they are always lower than the formal ones. In relation to SAHCs, theoretical studies have revealed that some charge transfer and electron sharing occurs when a metal is atomically dispersed on a carrier, these are mapped to the 'high-valent metal species' assigned by X-ray photoelectron spectroscopy.[11,28] However, this does not reflect the marginal differences in the calculated Bader charges and, in general, XPS low-valent metal species correspond to surface atoms and high-valent ones to isolated metals buried in the bulk of g-C_3N_4. Pt, Ir, Pd and Ag were all shown to be have a slight positive charge when isolated on g-C_3N_4.[17] For other polar carriers this assignment is easier, for example as Pt replaces Fe cations on the surface of Fe_2O_3 the resulting substitutional impurities carry considerable positive charges, which was linked to the remarkable CO oxidation activity of this catalyst.[1] Similarly, Pt was predicted to be trapped as Pt^{2+} on (100) nanofacets of CeO_2 and was detected as Pt^{2+} and Pt^{4+} (the corresponding Bader charges were not shown).[29] On the other hand, Au atoms located at the top sites of Pd_{55} nanoclusters were predicted to be negatively charged (-0.11 |e|).[30]

To gain insight into the role of the support, this work studies the effect of modifying the C/N ratio of g-C_3N_4 on the stabilisation, electronic properties and associated catalytic performance of palladium. For this purpose, a series of carbon-doped carriers were prepared by copolymerising the conventional cyanamide precursor with different amounts of barbituric acid (BA)[31,32]or 2,4,6-triaminopyrimidine (TAP)[33,34] (**Fig. 1**). To assess the effect of the surface area, the C-doped materials were prepared in bulk and mesoporous forms. In view of the widely-cited benefits in terms of enhanced size control and uniform dispersion, the introduction of palladium

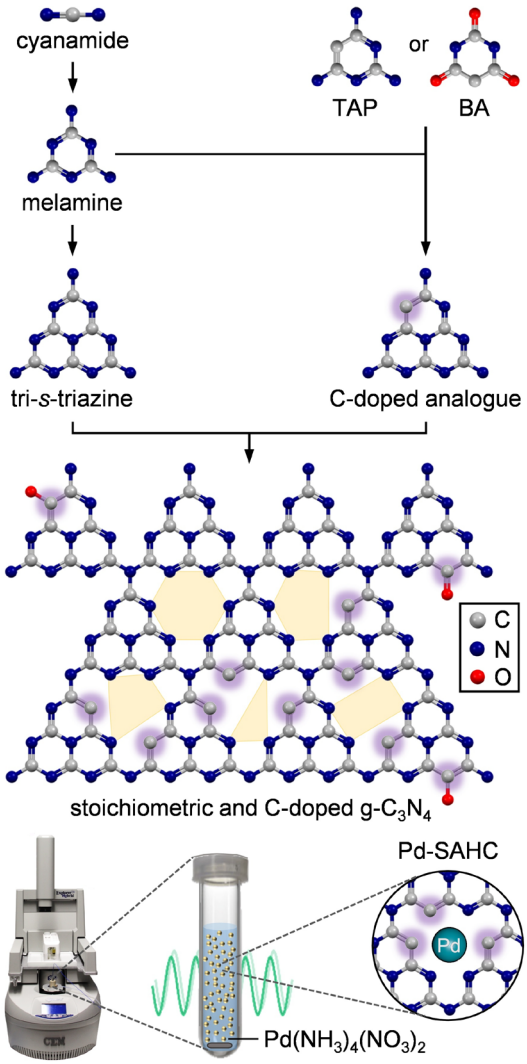

Fig. 1 Steps in the polymerisation of the stoichiometric and C-doped g-C_3N_4 and subsequent introduction of palladium by microwave-irradiation-assisted metal deposition. Additional C atoms in the modified lattice are highlighted by a purple glow. Yellow shaded areas connect N atoms within the coordination sites.

is subsequently approached *via* microwave-irradiation assisted-deposition. Characterisation by multiple techniques confirms the gradually increase C/N ratio of the carriers, that has a strong impact on the surface area, crystal size, thermal stability, and basic properties, and as a result, the ability to adsorb and stabilize single metal atoms. The latter was evaluated based on metal-carrier charge transfer, dispersion and areal density of the metal. Density functional theory calculations support the decreased adsorption energy of palladium in the C-doped lattice and highlight the potentially significant impact of oxygen-containing defects. To determine the influence on the catalytic efficiency, the resulting SAHCs were subsequently evaluated in the continuous-flow three-phased semi-hydrogenation of 2-methyl-3-butyl-2-ol, an important reaction in fine chemical and pharmaceutical manufacture.

Experimental

Carrier preparation

Bulk carbon nitride (BCN) was prepared by calcining dicyandiamide (10 g) at 823 K for 4 h (2.3 K min^{-1} ramp rate) under a nitrogen flow (15 cm^3 min^{-1}). Mesoporous carbon nitride (MCN) was prepared by adding cyanamide (2.5 g) to an aqueous dispersion of SiO_2 particles (40 wt.%, 12 nm diameter, Ludox HS-40) with an SiO_2:cynamide mass ratio of 1, and the mixture was stirred at 373 K until the water had completely evaporated. The resulting solids were ground with a mortar and pestle and then calcined as described for BCN. The silica template was subsequently removed by treating the resulting brown-yellow powder in an aqueous solution of NH_4HF_2 (4 M, 40 cm^3 g_{SiO2}^{-1}) for 48 h. The template-free MCN was then filtered, washed thoroughly with distilled water and ethanol and dried at 333 K overnight. Bulk (coded BCN-BA-*z*) and mesoporous (coded MCN-BA-*z* and MCN-TAP-*z*) C-doped materials were prepared by copolymerisation of cyanamide with barbituric acid (BA) or 2,4,6-triaminopyrimidine (TAP) in varying mass ratios ($z = 0.02$, 0.2 or 0.9) following the procedures described above. For reference, BA and TAP were carbonised in pure form (6 g) by calcination under the same conditions resulting in bulk BBA and BTAP materials.

Metal introduction

The incorporation of palladium into carriers was approached by postsynthetic microwave irradiation assisted deposition. The carrier (0.5 g) was firstly dispersed in H_2O (20 cm^3) with the assistance of sonication. Then, a solution of $Pd(NH_3)_4(NO_3)_2$ containing 5 wt.% Pd (50 μL) was added, targeting a metal loading of 0.5 wt.% relative to the carriers. The resulting solution was then placed in a microwave reactor (CEM Discover SP), applying a cyclic program of 15 s irradiation and 3 min cooling with 20 repetitions using a power of 100 W. The resulting powder was washed with distilled water and ethanol and dried at 333 K overnight.

Catalyst characterisation

Elemental analysis of C, H, N and O was determined by infrared spectroscopy using a LECO CHN-900 combustion furnace. Inductively coupled plasma-optical emission spectrometry (ICP-OES) was conducted using a Horiba Ultra 2 instrument equipped with photomultiplier tube detection. The solids were dissolved in a piranha solution and left under sonication until the absence of visible solids in the solution. Powder X-ray diffraction (XRD) was performed in a PANalytical X'Pert PRO-MPD diffractometer operated in Bragg Brentano geometry using Ni-filtered Cu Kα (λ = 0.1541 nm) radiation. Data were recorded in the range of 5-70° 2θ with an angular step size of 0.05° and a counting time of 2 s per step. The variation of the crystal size in the stacking direction was estimated from the broadening of the (002) reflection by using the Scherrer equation with a shape factor, $K = 0.9$. The interlayer staking distance was determined from the position of the (002) reflection using the Bragg equation. Nitrogen sorption was measured at 77 K in a Micrometrics 3Flex instrument, after evacuation of the samples at 423 K for 10 h. The pore size distribution was calculated using a non-local density functional theory (NLDFT) model for carbon with a slit-shaped pore geometry. X-ray photoelectron spectroscopy (XPS) was measured in a Physical Electronics Instruments Quantum 2000 spectrometer using monochromatic Al kα radiation generated from an electron beam operated at 15 kV and 32.3 W. The spectra were collected under ultra-high vacuum conditions (5×10^{-8} Pa) at a pass energy of 46.95 eV. All spectra were referenced to the N 1*s* peak of the ring nitrogen at 398.6 eV. ^{13}C solid-state cross-polarisation/magic angle spinning nuclear magnetic resonance (CP/MAS NMR) spectra were recorded on a Bruker AVANCE III HD NMR spectrometer at a magnetic field of 16.4 T corresponding to a ^1H Larmor frequency of 700.13 MHz. A 4 mm double resonance probe head at a spinning speed of 10 kHz was used for all experiments. The ^{13}C spectra were acquired using a cross polarisation experiment with a contact time of 2 ms and a recycle delay of 1 s. A total of 64×10^3 scans were added for each sample. Between 39×10^3 and 96×10^3 scans were acquired depending on the sample. ^{13}C experiments used high-power ^1H decoupling during acquisition using a SPINAL-64 sequence. Thermogravimetric analysis (TGA) was conducted in a Mettler Toledo TGA/DSC 1 Star system connected to a Pfeiffer Vacuum ThermoStar GSD 320 T1 Gas Analysis mass spectrometer. The analysis was performed in air or N_2 (40 cm^3 min^{-1}), heating the sample from 298 K to 1273 K at a rate of 5 K min^{-1}. The mass signals of H_2O (m/z = 18) and CO_2 (m/z = 44) were continuously monitored. Scanning electron microscopy (SEM) was undertaken in an FEI Magellan 400 microscope working at 30 kV and 50 pA. Samples for transmission electron microscopy (STEM) studies were prepared by dusting respective powders onto lacey-carbon coated copper grids. Conventional TEM imaging and STEM energy dispersive X-ray spectroscopy (EDX) measurements were performed on a Talos F200X instrument operated at 200 kV and equipped with an FEI SuperX detector. Aberration-corrected (AC-)STEM was performed using an FEI Titan Cubed microscope equipped with XFEG electron source and CEOS probe aberration corrector, operated at 300 kV. STEM high-angle annular dark-field (HAADF) images were acquired with an illumination angle of 17 mrad and detector inner angle of 35 mrad, chosen to minimise any possible Bragg diffraction contrast and maximise overall image signal, and especially atomic number (*Z*) contrast between Pd atoms/clusters and the underlying support. Per pixel dwell times of 5-10 μs and probe currents 40-60 pA were selected to achieve sufficient signal-to-noise for single Pd atom visibility whilst minimising beam induced changes, providing images representative of the Pd atom species and their distribution on the CN supports. Scanning electron micrographs of the uncoated samples were acquired using a Zeiss Gemini 1530 FEG SEM operated at 1 kV. CO_2 temperature-programmed desorption (CO_2-TPD) was carried out in a Micromeritics Autochem II 2920 equipped with a thermal conductivity detector coupled to MKS Cirrus 2 mass spectrometer. The samples were first activated at 473 K for 1 h under a helium atmosphere. Then the temperature was reduced to 323 K and the samples were saturated with CO_2 for

1.5 h before flushing with helium to remove physisorbed molecules. This procedure was repeated twice. Once the baseline was flat, the temperature was increased to 773 K at a rate of 10 K min^{-1} to obtain the CO_2 desorption curves. Diffuse reflectance infrared Fourier transform spectroscopy (DRIFTS) was performed using a Bruker Optics Vertex 70 spectrometer equipped with a high-temperature DRIFT cell (Harrick) and an HgCdTe (MCT) detector. Spectra were recorded in the range of 4000-400 cm^{-1} at room temperature under a N_2 flow by coaddition of 200 scans with a nominal resolution of 4 cm^{-1}.

Density functional theory

The Vienna *ab-initio* simulation package[35] was employed to model the structure of the Pd SAHCs based on the modified g-C_3N_4 carriers, using the Perdew–Burke–Ernzerhof functional together with dispersion terms D3.[36,37] The projector augmented wave method[38,39] was employed to represent core electrons and the valence was expanded in plane waves with a cutoff energy of 450 eV. The C_6N_8 (melon) moieties were built in a graphitic form and the optimised interlayer structure is 3.5 Å. Four layered slabs of the (0001) surface were built with *p*(2×2) supercells (**Fig. S13** and **S14**). The incorporation of metal atoms was assessed on one side of the slab.

Catalyst testing

The hydrogenation of 2-methyl-3-butyl-2-ol (Acros Organics, 98%) was carried out in a continuous-flow flooded-bed micro-reactor (ThalesNano H-Cube Pro™), in which the liquid feed (containing 5 vol.% of substrate and toluene (Fischer Chemicals, 99.95%) and gaseous hydrogen (generated *in situ* by Millipore water electrolysis) flow concurrently upward through a cylindrical cartridge (3.5 mm internal diameter) containing a fixed bed of catalyst (0.1 g) and silicon carbide (0.12 g) particles, both with a size of 0.2-0.4 mm. The reactions were conducted at various conditions of temperature (303-363 K), total pressure (1-8 bar), liquid (1 cm^3 min^{-1}) and H_2 (40 cm^3 min^{-1}) flow rates. The products were collected every 15 min after reaching steady state and analysed offline using a gas chromatograph (HP-6890) equipped with a HP-5 capillary column and a flame ionisation detector. The conversion (*X*) of the substrate was determined as the amount of reacted substrate divided by the amount of substrate at the reactor inlet. The selectivity (*S*) to each product was quantified as the amount of the particular product divided by the amount of reacted substrate. The reaction rate (*r*) was expressed as moles of product per mole of Pd and unit of time.

Results and Discussion

Carrier properties

The preparation of carbon-doped g-C_3N_4 carriers was approached by copolymerising the conventional cyanamide precursor with barbituric acid (BA) or 2,4,6-triaminopyrimidine (TAP). These compounds both contain carbon-rich heterocycles with respect to the six-membered ring of melamine, the smallest aromatic unit of the condensed structure of graphitic carbon nitride, and ideally have

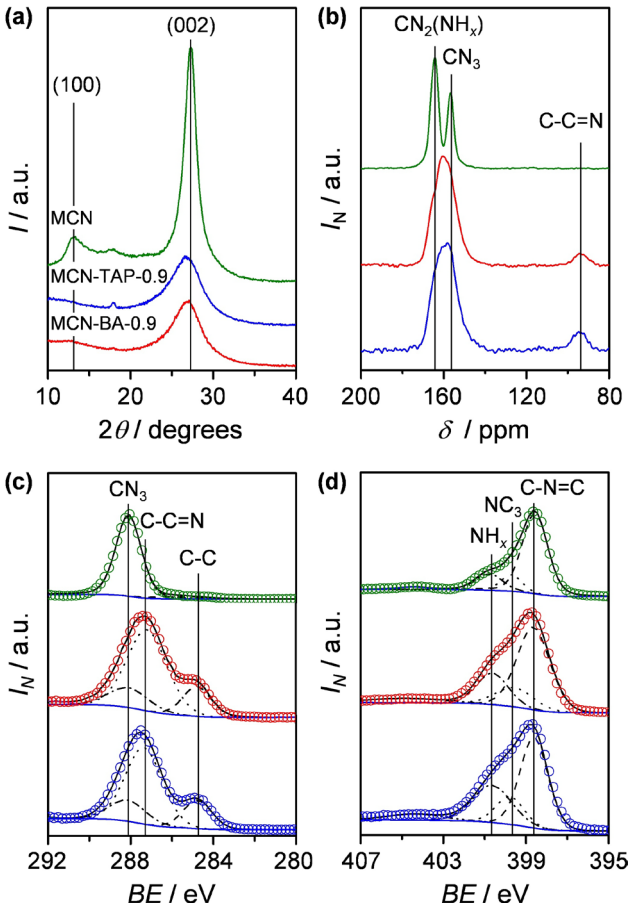

Fig. 2 (a) XRD patterns, (b) ^{13}C MAS NMR spectra, (c) C 1*s* XPS spectra and (d) N 1*s* XPS spectra of the stoichiometric and C-doped mesoporous g-C_3N_4 carriers. In (c,d), solid black lines show the result of fitting the raw data (open symbols), the dashed lines correspond to the individual peaks after deconvolution. Blue lines indicate the background applied.

compatible functionality to copolymerise with this molecule to form the standard tri-*s*-triazine units *via* the elimination of ammonia or water.[31-34] To demonstrate the flexibility of this approach and to study the impact of surface area, C-doped carriers have been prepared in both bulk and mesoporous forms, the latter obtained by applying colloidal silica as a hard template during the synthesis. The resulting samples are coded *x*-*y*-*z*, where *x* denotes the carrier morphology (bulk - BCN or mesoporous - MCN), *y* corresponds to the dopant applied (BA or TAP) and *z* indicates the cyanamide/dopant mass ratio (0.02, 0.2 or 0.9). For reference purposes, the stoichiometric g-C_3N_4 carrier was also synthesised in bulk (BCN) and mesoporous (MCN) form and the individual dopants were also polymerised in bulk form leading to the BBA and BTAP materials.

Various techniques were applied to characterise the properties of the modified carriers. The framework composition of all carriers was determined based on elemental analysis after correction for the possible adsorption of gases by the material (*vide infra*). Upon introduction of BA or TAP during the synthesis an increased amount of carbon is observed (**Table S1**), consistently, the C/N ratio rises from 0.6 in the stoichiometric materials to close to 1 in the C-doped analogues. Comparison of the X-ray diffraction (XRD) patterns

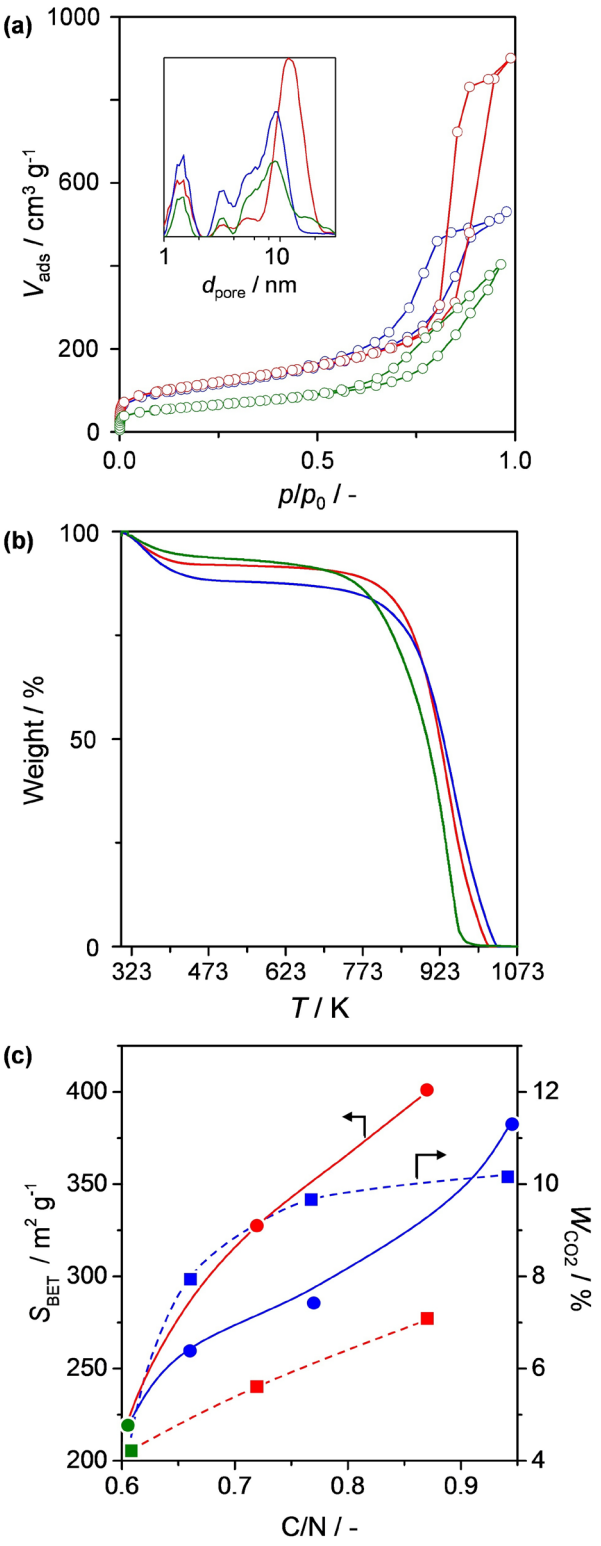

Fig. 3 (a) N_2 isotherms and corresponding NLDFT pore size distributions (inset), (b) TGA profiles in air and (c) the variation of the BET surface area (circles) and the amount of CO_2 adsorbed (squares) with the C/N ratio of the stoichiometric MCN (green) and C-doped carriers modified with TAP (red) and BA (blue).

of the mesoporous (**Fig. 2**) and bulk (**Fig. S1**) carriers reveals that the incorporation of carbon was accompanied by a disturbance of the graphitic carbon nitride lattice. In particular, increasing the cyanamide/dopant ratio was associated with a broadening and reduced intensity of the (002) stacking reflection at $2\theta = 27.3°$ (**Fig. S2**). Moreover, the (100) reflection at $2\theta = 13.1°$ corresponding to the in-plane order of tri-*s*-triazine units within the g-C_3N_4 sheets, is not visible in the carbon-doped samples, suggesting an increased distortion of g-C_3N_4 layers.[40] Estimation using the Scherrer equation (**Table S2**), confirmed a decrease of the crystal size in the stacking direction of the lattice with increasing C/N ratio from 9 nm in the stoichiometric MCN carrier to 2 nm in MCN-TAP-0.9 and MCN-BA-0.9 (**Fig. S3**), indicating that the presence of both dopants hinders the polymerisation of cyanamide. Note that the values of crystal size should only be used for qualitative comparison since doping of the lattice with carbon can also introduce lattice distortion and structural defects leading to peak broadening, which is difficult to decouple from the purely size related effect. The slight shift of the (002) reflection indicates a small concomitant increase in the interlayer stacking from 0.326 nm in MCN to 0.332 nm in MCN-BA-0.9.[34] In fact, the substitution of one or more nitrogen atoms in the framework of g-C_3N_4 leads to a decreased strength of hydrogen bonds, which is known to reduce the stability and structural regularity in g-C_3N_4 materials.[32] Comparatively, the observation of a single broad reflection at $2\theta = 27.3°$ in the materials obtained upon the direct thermal condensation of barbituric acid (BBA) or 2,4,6-triaminopyrimidine (BTAP) indicates that they adopt a layered structure similar to that of the conventional graphitic carbon nitride (BCN).

To further confirm the successful incorporation of carbon into the g-C_3N_4 lattice, the mesoporous samples were studied by magic-angle spinning nuclear magnetic resonance (MAS NMR) and X-ray photoelectron (XPS) spectroscopy. The two main signals at 164 and 157 ppm in the ^{13}C MAS NMR spectrum of MCN are attributed to $CN_2(NH_x)$ and CN_3 moieties, respectively (**Fig. 2b**).[41] The gradual coalescence of these peaks with increased amount of BA or TAP (**Fig. S4**) can be related to

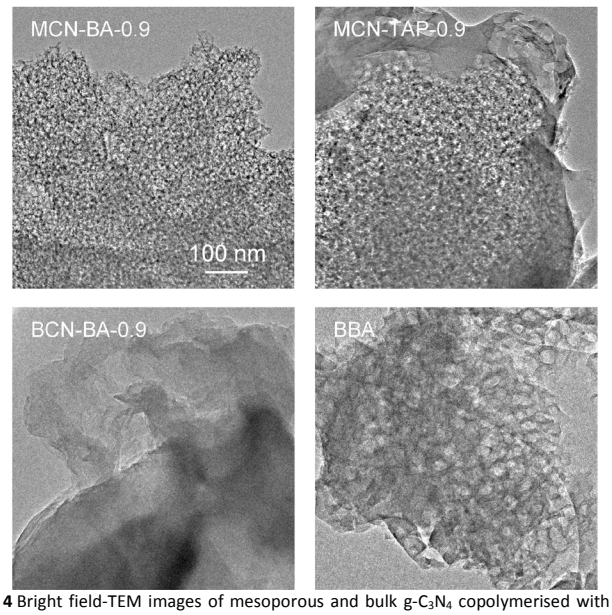

Fig. 4 Bright field-TEM images of mesoporous and bulk g-C_3N_4 copolymerised with BA or TAP. The 100 nm scale bar applies to all images.

the decreased crystalline order of the tri-*s*-triazine moieties. In addition, a new peak centred at 95 ppm appears, which reflects the desired incorporation of -C-C=N- units into the framework.[32] Consistently, MCN-BA-0.9 and MCN-TAP-0.9 samples evidence a strong peak at 287.3 eV in the C 1*s* XPS spectra (**Fig. 2c**) that is attributed to C-doped -C-C=N- moieties,[42] while the peak at 284.8 eV that represents C-C bond formation also increases. The latter could result from the formation of an amorphous carbon phase during the polymerisation.[43] The existence of the tri-*s*-triazine units was confirmed by the presence of the peak at 288.1 eV (CN_3).[44] Deconvolution of N 1*s* XPS spectra (**Fig. 2d**) identifies the presence of nitrogen species, typical for the g-C_3N_4 structure. Three main peaks at 398.6 eV (ring nitrogen, C-N=C), 399.5 eV (tertiary nitrogen, NC_3) and 400.6 eV (NH_x groups) are observed in all spectra. The presence of tertiary nitrogen and the C-N=C/NC_3 ratio of 6 for MCN carrier confirms that the structure is based on tri-*s*-triazine building block.[45] The C-N=C/NC_3 ratio drops to 3.7 and 3.5 for MCN-TAP-0.9 and MCN-BA-0.9, respectively, indicating a decreased amount of the ring nitrogen in the carbon-doped carriers and evidencing the successful substitution of nitrogen by carbon in the sixfold cavity of the g-C_3N_4 structure.

As evidenced by nitrogen sorption (**Fig. 3a**), MCN-BA-0.9 and MCN-TAP-0.9 display an enhanced surface area compared to pure MCN (**Table S2**). The prominent hysteresis loops observed in all isotherms evidence the presence of connected spherical or cylindrical mesopores. Corresponding pore size distributions (**Fig. 3a**, inset) display two pronounced peaks, centred at 1.5 and 10 nm, the latter close to the size of the SiO_2 template. The increased surface area with increasing C/N ratio is in agreement with the reduced crystalline order. Interestingly, distinctions are visible between the application of BA and TAP (**Fig. S3**), the former resulting in a greater enhancement in the surface area with decreasing crystal size. As expected, the BCN and BTAP carriers exhibit surface areas lower than 10 $m^2 g^{-1}$ consistent with the densification of the polymerised structures in the absence of a template. In comparison, BBA and BCN-BA-0.9 display relatively high specific surface areas of 45 and 48 $m^2 g^{-1}$, respectively, with a hysteresis loop at p/p_0 = 0.3-0.9, suggesting the presence of smaller crystalline domains and/or a higher number of defects in these samples (**Fig. S1**). Examination of the carriers by transmission electron microscopy (TEM) demonstrates that the inclusion of BA or TAP does not radically alter the morphology up to a mass ratio of 0.9 (**Fig. 4** and **S5**). All mesoporous carriers exhibit the extensive presence of spherical mesopores of sizes around that of the 12 nm diameter of the colloidal silica template, while the bulk carriers exhibit a reduced more uniform beam transparency. Scanning electron microscopy (SEM) images of MCN also reveal the presence of macropores with the size of around 500 nm, which are not observed in the large particles of BCN. Analysis by selected area electron diffraction confirmed the polycrystalline nature of the material (**Fig. S5**). Note that the observation of large meso-/macropores in BBA agrees with the higher surface area of this material.

The impact of carbon doping on the thermal stability of the carrier and the propensity to adsorb gases was assessed by thermogravimetric analysis (TGA) in air and in nitrogen, respectively, following the evolution of volatile species by mass spectrometry (MS). The thermal stability was improved after carbon introduction. For example, the temperature for 50% weight loss of MCN-BA-0.9 or MCN-TAP-0.9 is 50 K higher compared to MCN (**Fig. 3b** and **S2**), which also applies for the bulk carriers (**Fig. S1**). In line with the fact that carbon nitride is weakly basic and has previously been studied for CO_2 capture, weight losses below 573 K primarily resulted from the desorption of CO_2 (**Fig. S6**). Consistent with the enhanced surface area, a strong correlation was observed between the CO_2 uptake and the C/N ratio of the carrier (**Fig. 3c**). Interestingly, a more significant increase resulted upon modification with BA that TAP, suggesting possible differences in the basicity of these samples. To study this, temperature-programmed reduction measurements of CO_2 (CO_2-TPD) monitored by MS were conducted. Two desorption peaks were observed in the CO_2-TPD profiles, the first centred at 373 K (**Fig. S7**) corresponding to the presence of weak Lewis basicity[46] and as second broader peak around 533 K, attributed to stronger basic sites. Comparatively, MCN-TAP-0.9 was seen

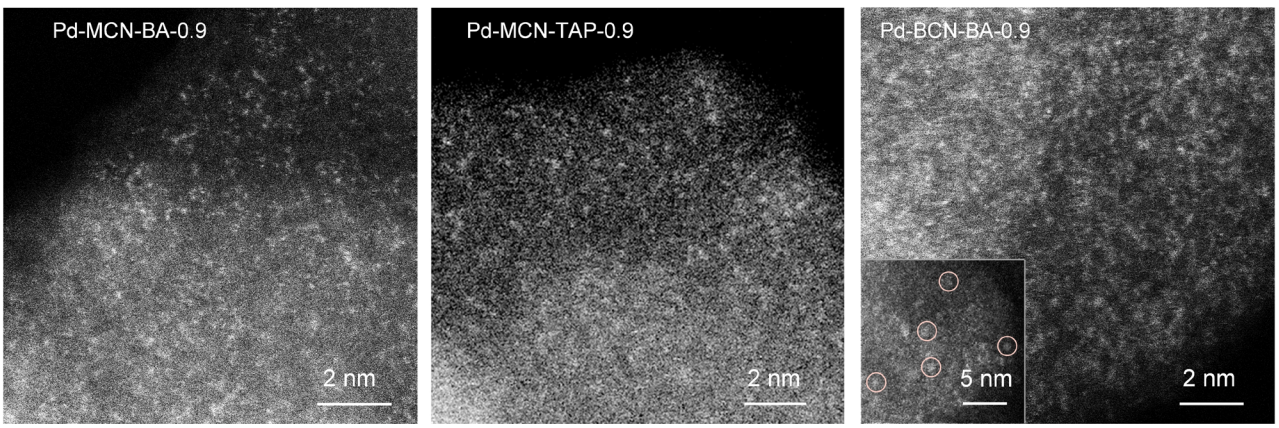

Fig. 5 AC-STEM images of the metal speciation in Pd-containing SAHCs based on the C-doped carriers, evidencing single atom dispersion. Pd-BCN-BA-0.9 also contains small *ca.* 1 nm clusters, as highlighted inset.

to exhibit a higher concentration of weak basic sites, while MCN-BA-0.9 contained more strong basic sites, which can explain the higher CO_2 uptake of the latter sample.

Based on the amount of CO_2 adsorbed it is clear that this accounts for the majority of oxygen detected by elemental analysis. Correction of the chemical composition reveals that the amount of oxygen in the lattice of the C-doped carriers is relatively low (<2.4 mol%) and is not significantly impacted by the presence of mesoporosity. The fact that no adsorbed H_2O was detected indicates that the hydrogen evidenced in the carriers most likely relates to defects such as tertiary or secondary amines. Attempts to identify the possible origin of oxygen-related defects by assessment of the surface properties by diffuse reflectance infrared Fourier transform spectroscopy (DRIFTS) were complicated by the overlapping signals associated with the g-C_3N_4 lattice (**Fig. S8**). Nonetheless, comparison of the spectra did confirm higher numbers of secondary amine defects in the C-doped carriers with respect to the stoichiometric MCN.

Palladium stabilisation on the carriers

The stabilisation of palladium on the carriers *via* microwave-irradiation-assisted deposition attained a metal loading close to the targeted value of 0.5 wt.% in all cases (**Table S3**). Careful examination of the metal speciation by aberration-corrected (AC-)STEM, confirmed the single atom dispersion (**Fig. 5** and **S9**) and the absence of Pd nanoparticles in all of the catalysts based on the mesoporous C-doped carriers (as summarised in **Table S3**). Energy-dispersive X-ray spectroscopy (EDX) mapping also supported the uniformity of the Pd distribution over these carriers (**Fig. S10**). However, some metal clusters of ~1 nm were observed in Pd-BCN-BA-0.9 (**Fig. 5**, inset). High metal dispersions were also observed in Pd-BCN (**Fig. S11**). This is noteworthy as previous attempts at depositing palladium on BCN led to significant nanoparticle formation,[17] pointing toward the benefits of using microwave-irradiation to improve the stabilisation of single atoms on low surface area carriers In contrast, extensive formation of Pd clusters and small nanoparticles was evidenced in Pd-BBA, which has the highest surface area of the bulk carriers (61 $m^2\ g^{-1}$). Thus, the metal speciation appears to be more strongly dependent on the structure and binding strength of the coordination sites within the material rather than the surface area. Since the polymerisation of BA and TAP does not result in crystalline materials based on tri-*s*-triazine networks, these carriers behave more like nitrogen-doped carbons and are unable to effectively stabilise isolated metal centres

Further insight into the interaction of palladium with the C-doped carriers was obtained by analysis by X-ray photoelectron spectroscopy (XPS), which enabled comparison of the impact of varying the composition on the surface concentration ($Pd_{surface}$) and formal oxidation state of the metal (**Fig. 6a** and **S12**). Surface enrichment of Pd was observed in all samples (**Table S3**), which agrees with the high barriers for the diffusion of Pd atoms into sub-subsurface layers predicted by previous DFT calculations.[17] In line with the higher local surface metal concentrations experienced during the synthesis, much more drastic increases in $Pd_{surface}$ were observed in catalysts based on the low-surface bulk carriers (11-24 times) with respect to the mesoporous analogues (2-4 times). Nonetheless, opposite behaviour is observed on comparison of the series of catalysts based on the mesoporous C-doped carriers, which display an appreciable increase in $Pd_{surface}$ with surface area (**Fig. 6b**). This suggests that doping the lattice with carbon either hinders the diffusion of palladium into subsurface layers or creates stronger adsorption sites at the surface with respect to the stoichiometric lattice.

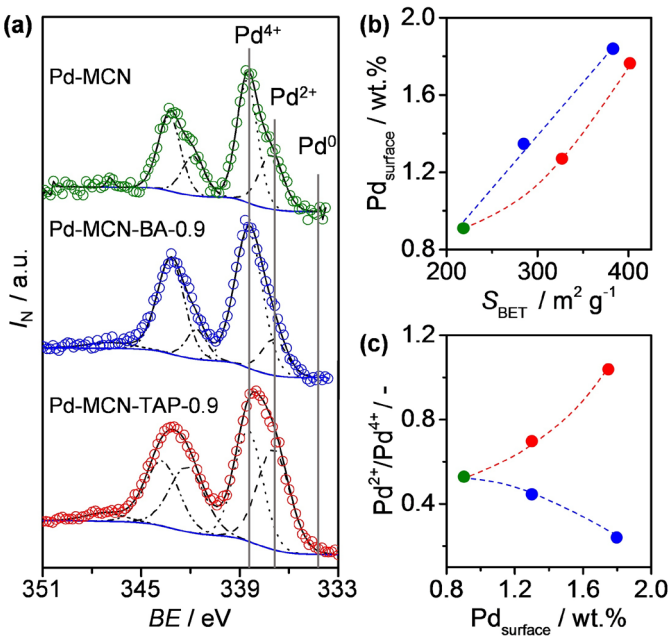

Fig. 6 (a) Comparison of the Pd 3*d* core level XPS spectra of the catalysts based on the mesoporous carriers. Solid black lines show the result of fitting the raw data (open symbols), the dashed lines correspond to the individual peaks after deconvolution. Blue lines indicate the background applied. Vertical grey lines correspond to the deconvoluted components, which are assigned based on the shifts expected for bulk species. (b) The correlation between Pd surface concentration and BET surface area. (c) The correlation between Pd^{2+}/Pd^{4+} ratio and Pd surface concentration. In (b), (c) and the intermediate samples MCN-BA-0.2 and MCN-TAP-0.2 are included. Green symbol refers to the MCN carrier, while red and blue symbols denote carriers modified with TAP and BA, respectively.

Deconvolution of the Pd $3d_{5/2}$ spectra identified two peaks at 338.5 eV and 336.9 eV in all samples (**Fig. 6a**), which are tentatively assigned to Pd^{4+} and Pd^{2+}, respectively. Notably, no peak corresponding to metallic Pd around 335.0 eV was observed in any of the spectra.[47] Interestingly, significant variation is observed in the relative peak intensity, the Pd^{2+}/Pd^{4+} ratio changing from 0.24 for Pd-MCN-BA-0.9 to 1.04 for Pd-MCN-TAP-0.9, while Pd-MCN shows intermediate value 0.53 (**Table S3**). Replacing the nitrogen atoms with carbon in the stoichiometric g-C_3N_4 structure, a weaker metal-carrier interaction, which is corroborated by the reduced adsorption energies of isolated Pd atoms by 0.2-0.5 (*vide infra*) and thus a higher Pd^{2+}/Pd^{4+} ratio is expected, as in the case of Pd-MCN-TAP-0.9. In contrast to this, a lower Pd^{2+}/Pd^{4+} ratio was observed in Pd-MCN-BA-0.9. Attempts to correlate the differences in the relative amounts of high- and low-valent metal with a bulk compositional parameter (*e.g.*, the C/N ratio,

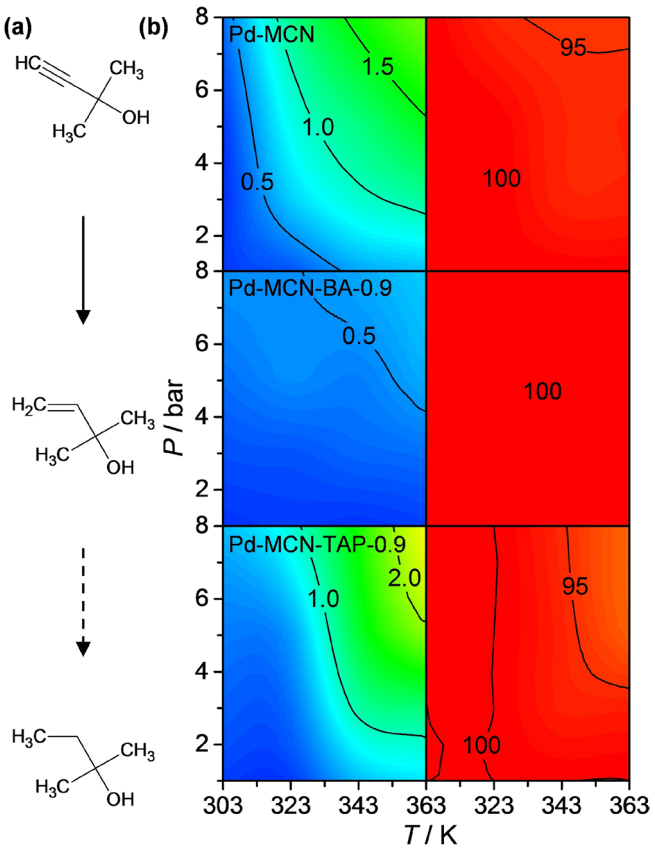

Fig. 7 (a) Reaction scheme of the selective hydrogenation of 2-methyl-3-butyn-2-ol to 2-methyl-3-buten-2-ol and the unselective over-hydrogenation to 2-methyl-3-butan-2-ol. (b) Reaction rate (left column, in 10^3 $mol_{2\text{-methyl-3-buten-2-ol}}$ mol_{Pd}^{-1} h^{-1}) and selectivity to 2-methyl-3-buten-2-ol (right column, in %) at different temperature and pressure over Pd-based catalysts on g-C_3N_4. The contour plots were obtained through spline interpolation of 14 experimental points. Reaction conditions: W_{cat} = 0.1 g, F_L (2-methyl-3-butyn-2-ol + toluene) = 1 cm^3 min^{-1} and F_G (H_2) = 36 cm^3 min^{-1}.

O content or lattice electronegativity) did not uncover any general relationship. This is perhaps unsurprising considering that the metal is primarily located in the surface layers of the carrier and therefore most likely to depend on the specific termination of the lattice and presence of surface defects. The distinct variations in the CO_2 uptake and basicity of the C-doped carriers already points towards differences in the surface properties depending on the dopant applied. Importantly, comparison of the Pd^{2+}/Pd^{4+} ratio *versus* $Pd_{surface}$ confirms that the variation does not result from differences in the areal density of palladium between the samples (**Fig. 6c**). The absence of the metallic Pd signal in the Pd 3*d* spectra of Pd-BBA and Pd-BTAP conflicts with the presence of small clusters as confirmed by STEM analysis, which can be explain by bathochromic shift due to the quantum effects appears for particles smaller than 2 nm.[27] These results highlight the current analytical challenges faced to describe the metal-carrier interaction with respect to understanding both the XPS response and the precise surface structure.

Modelling

To gain molecular insight into the impact of carbon doping on the interaction of palladium with carbon nitride, density functional theory (DFT) calculations have been carried out for the binding sites defined by the tri-*s*-triazine (C_6N_8) units considering two possible stacking arrangements (**Fig. S13**). As illustrated in **Fig. S14**, chemical defects have been incorporated into the structure by replacing some of the nitrogen atoms by CH or by CO and a nearby H. The former comprises the targeted substitution in the C-doped structures, while the latter represents a possible type of oxygen-containing defect that may form due to the oxidation of the material during synthesis.[48] The metal stabilisation was subsequently studied by placing Pd atoms at different depths within the modified interstices (**Fig. S14**).

The adsorption of palladium in the stoichiometric (defect-free) compound ranges from 2 eV for the bulk of the material to 1.7 eV at the surface. C-doped materials are less prone to adsorb Pd and the adsorption energy is reduced by 0.25-0.5 eV on the surface close to a defect (**Table S4**). The computed XPS shifts show that the analysis is complex. The 3*d* levels of Pd atoms adsorbed at the surface are shifted towards smaller binding energies by about 0.4 eV. Thus, qualitative analysis of the XPS data indicates that both Pd^{4+}-like (in the bulk) and Pd^{2+}-like (at the surface) atoms can be formed. However, calculated Bader charges are small (*ca.* 0.5|e^-|) due to the large covalency between the metal atom and the lattice. The C-doped structures present similar features, but with one noticeable difference in the XPS signature related to Pd in close contact with O defects. Pd adsorbed in these sites are closer to the Pd^{4+} feature, exhibiting -0.50 eV higher binding energies with respect to Pd atoms in the bulk of the stoichiometric C_3N_4 reference. Comparatively, the weakest interaction is identified upon replacing N with a CH defect, while close to an O-defect Pd atoms are more stable with respect to the stoichiometric sites. This implies that Pd is better anchored at the O-defect sites in a strongly cationic configuration, which could explain the higher Pd^{4+}/Pd^{2+} ratios observed in the BA-modified materials, whereas the TAP-modified carriers behave more like an ideal C-doped carbon nitride due to the lower adsorption energy, leading to a higher concentration of "effective" palladium close to the surface.

Catalytic performance

The performance of the Pd-SAHCs based on the C-doped carriers was evaluated in the continuous-flow semi-hydrogenation of 2-methyl-3-butyn-2-ol (**Fig. 7a**). To decouple the impact of the carrier composition, the tests focused on the catalysts based on the mesoporous carriers, which exclusively contain isolated Pd atoms in comparably low areal density (0.47±0.09 μmol_{Pd} m^{-2}). The contour maps in **Fig. 7b** depict the rate and selectivity to 2 methyl-3-buten-2-ol over selected catalysts at different temperatures and pressures. Under the conditions investigated, the conversion of 2-methyl-3-butyn-2-ol ranged between 3 and 60% in all cases. The high chemoselectivity of the single atoms was clearly evidenced by the selectivity to the alkenol product in excess of 95%. Interestingly, the application of BA or TAP to prepare C-doped carriers is seen to have opposite effects;

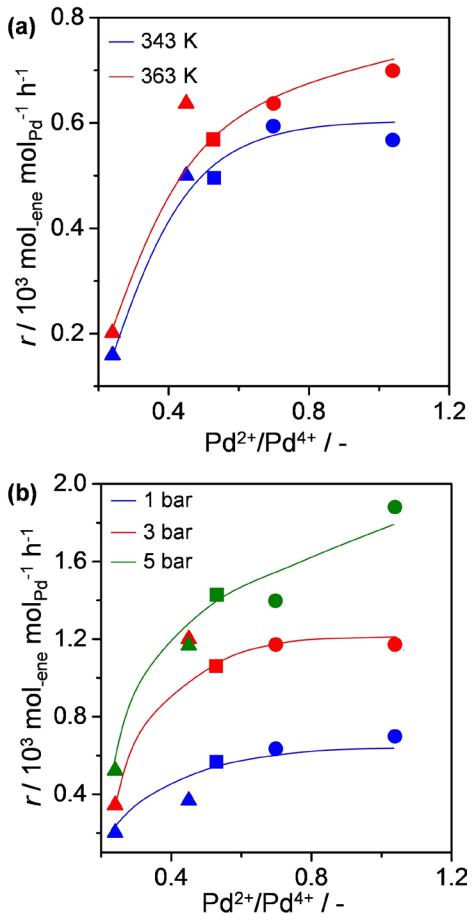

Fig. 8 Correlation of the rate of alkenol formation in the semi-hydrogenation of 2-methyl-3-butyn-2-ol as a function of the (a) temperature (P = 1 bar) or (b) pressure (T = 363 K) of reaction with the Pd^{2+}/Pd^{4+} ratio over Pd-MCN (squares) or over the SAHCs based on the mesoporous C-doped carriers modified with BA (triangles) or TAP (circles).

Pd-MCN-BA-0.9 appears less active than Pd-MCN, while higher rates are achieved over Pd-MCN-TAP-0.9.

Comparison of the rate or alkenol formation over all of the mesoporous SAHCs as a function of the Pd^{2+}/Pd^{4+} ratio at different temperatures (**Fig. 8a**) and pressures (**Fig. 8b**) reveals a strong dependence on the relative amount of the lower-valent metal species. In particular, at 1 bar and 343 K, the conditions of highest practical relevance, over a 3-fold variation in the reaction rate is observed. Tests of selected catalysts based on the bulk carbon nitride evidenced significantly higher rates than those observed over the SAHCs based on the mesoporous carriers (**Fig. S15**), which can be attributed to the much higher surface density of metal in these samples (110 and 15.5 μmol_{Pd} m^{-2} for Pd-BCN-BA-0.9 and Pd-BBA respectively). Despite containing visible Pd nanoclusters, Pd-BCN-BA-0.9 preserved fully selective character to the alkenol. In contrast, a high degree of overhydrogenation was evidenced over Pd-BBA, which is ascribed to the extensive formation of Pd clusters and small nanoparticles. These findings point toward the importance of tuning the metal-carrier interaction for the design of highly efficient SAHCs. The significant variation in the surface density of metal and the heterogeneous metal speciation present significant challenges for the comparative evaluation of catalysts based on the bulk carriers. In particular, the difficulty in quantifying the amount and properties of nanoclusters and single atoms, which cannot be assessed by standard chemisorption techniques, highlights the need for improved methods to precisely control and characterise the distribution and dispersion of metals in g-C_3N_4.

Conclusions

This study has assessed the impact of varying the elemental composition of graphitic carbon nitride on the stabilisation and catalytic efficiency of palladium species on this carrier. Controlled modification of the C/N ratio could be achieved by the copolymerisation of cyanamide with carbon-rich heterocycles. The substitution of nitrogen by carbon in the lattice was confirmed by elemental analysis, XPS and ^{13}C NMR spectroscopy and was found to concomitantly enhance the surface area and thermal stability. Microwave-irradiation-assisted deposition was shown to be an effective route for dispersing metals as single atoms even on low surface area carriers. As evidenced by XPS and AC-STEM, both the speciation and oxidation state of palladium was influenced by the specific dopant applied. The incorporation of 2,4,6-triaminopyrimidine led to the weakening of the metal-carrier interaction expected due to the reduced coordination number of the binding sites, but an increased binding strength was observed upon incorporation of barbituric acid. Experimental and theoretical observations pointed towards differences in the surface properties, possibly related to the presence of oxygen-related defects. The metal oxidation state assigned from XPS in the resulting catalysts was found to be an important indicator for the semi-hydrogenation of 2-methyl-3-butyn-2-ol with an enhanced catalytic efficiency observed over catalysts containing higher fractions of lower-valence Pd^{2+} species, which according to the calculations correspond to Pd atoms at the surface or near CH defects. The findings demonstrate the possibility of improving the efficiency of SAHCs by tailoring the carrier properties.

Acknowledgements

This research has received funding from the Swiss National Science Foundation (Grant No. 200021-169679) as well as the European Research Council under the European Union's Seventh Framework Programme (FP7/2007–2013)/ERC grant agreement 291522–3DIMAGE and the European Union Seventh Framework Programme under Grant Agreement 312483-ESTEEM2 (Integrated Infrastructure Initiative -I3). Dr Réne Verel (ETH Zurich) is thanked for assistance with ^{13}C MAS-NMR. ScopeM at ETH Zurich is acknowledged for providing access to its facilities. R.K.L. acknowledges a Junior Research Fellowship from Clare College.

References

1. B. Qiao, A. Wang, X. Yang, L. F. Allard, Z. Jiang, Y. Cui, J. Liu, J. Li and T. Zhang, *Nat. Chem.*, 2011, **3**, 634-641.
2. X.-F. Yang, A. Wang, B. Qiao, J. Li, J. Liu and T. Zhang, *Acc. Chem. Res.*, 2013, **46**, 1740-1748.
3. S. Liang, C. Hao and Y. Shi, *ChemCatChem*, 2015, **7**, 2559-2567.
4. G. Kyriakou, M. B. Boucher, A. D. Jewell, E. A. Lewis, T. J. Lawton, A. E. Baber, H. L. Tierney, M. Flytzani-Stephanopoulos and E. C. H. Sykes, *Science*, 2012, **335**, 1209-1212.
5. J. M. Thomas, *Nature*, 2015, **525**, 325-326.
6. M. Moses-DeBusk, M. Yoon, L. F. Allard, D. R. Mullins, Z. Wu, X. Yang, G. Veith, G. M. Stocks and C. K. Narula, *J. Am. Chem. Soc.*, 2013, **135**, 12634-12645.
7. Q. Fu, H. Saltsburg and M. Flytzani-Stephanopoulos, *Science*, 2003, **301**, 935-938.
8. Y. Zhai, D. Pierre, R. Si, W. Deng, P. Ferrin, A. U. Nilekar, G. Peng, J. A. Herron, D. C. Bell, H. Saltsburg, M. Mavrikakis and M. Flytzani-Stephanopoulos, *Science*, 2010, **329**, 1633-1636.
9. S. Sun, G. Zhang, N. Gauquelin, N. Chen, J. Zhou, S. Yang, W. Chen, X. Meng, D. Geng, M. N. Banis, R. Li, S. Ye, S. Knights, G. A. Botton, T.-K. Sham and X. Sun, *Sci. Rep.*, 2013, **3**, 1775.
10. A. Uzun, V. Ortalan, Y. Hao, N. D. Browning and B. C. Gates, *ACS Nano*, 2009, **3**, 3691-3695.
11. M. Yang, J. Liu, S. Lee, B. Zugic, J. Huang, L. F. Allard and M. Flytzani-Stephanopoulos, *J. Am. Chem. Soc.*, 2015, **137**, 3470-3473.
12. A. L. Yakovlev, K. M. Neyman, G. M. Zhidomirov and N. Rösch, *J. Phys. Chem.*, 1996, **100**, 3482-3487.
13. J. Lin, A. Wang, B. Qiao, X. Liu, X. Yang, X. Wang, J. Liang, J. Li, J. Liu and T. Zhang, *J. Am. Chem. Soc.*, 2013, **135**, 15314-15317.
14. H. Wei, X. Liu, A. Wang, L. Zhang, B. Qiao, X. Yang, Y. Huang, S. Miao, J. Liu and T. Zhang, *Nat. Commun.*, 2014, **5**, 5634.
15. Z. Zhao, Y. Sun and F. Dong, *Nanoscale*, 2015, **7**, 15-37.
16. Y. Zheng, J. Liu, J. Liang, M. Jaroniec and S. Z. Qiao, *Energy Environ. Sci.*, 2012, **5**, 6717-6731.
17. Z. Chen, S. Mitchell, E. Vorobyeva, R. K. Leary, R. Hauert, T. Furnival, Q. M. Ramasse, J. M. Thomas, P. A. Midgley, D. Dontsova, M. Antonietti, S. Pogodin, N. López and J. Pérez-Ramírez, *Adv. Funct. Mater.*, 2017, **27**, 1605785.
18. X. Huang, Y. Xia, Y. Cao, X. Zheng, H. Pan, J. Zhu, C. Ma, H. Wang, J. Li, R. You, S. Wei, W. Huang and J. Lu, *Nano Res.*, 2017, DOI: 10.1007/s12274-016-1416-z, 1-11.
19. Z. Chen, S. Pronkin, T.-P. Fellinger, K. Kailasam, G. Vilé, D. Albani, F. Krumeich, R. Leary, J. Barnard, J. M. Thomas, J. Pérez-Ramírez, M. Antonietti and D. Dontsova, *ACS Nano*, 2016, **10**, 3166-3175.
20. X. Li, W. Bi, L. Zhang, S. Tao, W. Chu, Q. Zhang, Y. Luo, C. Wu and Y. Xie, *Adv. Mater.*, 2016, **28**, 2427-2431.
21. S. J. Tauster, S. C. Fung, R. T. K. Baker and J. A. Horsley, *Science*, 1981, **211**, 1121-1125.
22. G. N. Vayssilov, Y. Lykhach, A. Migani, T. Staudt, G. P. Petrova, N. Tsud, T. Skála, A. Bruix, F. Illas, K. C. Prince, V. Matolín, K. M. Neyman and J. Libuda, *Nat. Mater.*, 2011, **10**, 310-315.
23. A. Kumar and V. Ramani, *ACS Catal.*, 2014, **4**, 1516-1525.
24. F. Besenbacher, I. Chorkendorff, B. S. Clausen, B. Hammer, A. M. Molenbroek, J. K. Nørskov and I. Stensgaard, *Science*, 1998, **279**, 1913-1915.
25. F. R. Lucci, J. Liu, M. D. Marcinkowski, M. Yang, L. F. Allard, M. Flytzani-Stephanopoulos and E. C. H. Sykes, *Nat. Commun.*, 2015, **6:8550**.
26. M. Mavrikakis, P. Stoltze and J. K. Nørskov, *Catal. Lett.*, 2000, **64**, 101-106.
27. Y. Sun, Y. Wang, J. S. Pan, L.-l. Wang and C. Q. Sun, *J. Phys. Chem. C*, 2009, **113**, 14696-14701.
28. G. Vilé, D. Albani, M. Nachtegaal, Z. Chen, D. Dontsova, M. Antonietti, N. López and J. Pérez-Ramírez, *Angew. Chem. Int. Ed.*, 2015, **54**, 11265-11269.
29. A. Bruix, Y. Lykhach, I. Matolínová, A. Neitzel, T. Skála, N. Tsud, M. Vorokhta, V. Stetsovych, K. Ševčíková, J. Mysliveček, R. Fiala, M. Václavů, K. C. Prince, S. Bruyère, V. Potin, F. Illas, V. Matolín, J. Libuda and K. M. Neyman, *Angew. Chem. Int. Ed.*, 2014, **53**, 10525-10530.
30. H. Zhang, T. Watanabe, M. Okumura, M. Haruta and N. Toshima, *Nat. Mater.*, 2012, **11**, 49-52.
31. M. Shalom, M. Guttentag, C. Fettkenhauer, S. Inal, D. Neher, A. Llobet and M. Antonietti, *Chem. Mater.*, 2014, **26**, 5812-5818.
32. J. Zhang, X. Chen , K. Takanabe, K. Maeda, K. Domen, J. D. Epping, X. Fu, M. Antonietti and X. Wang, *Angew. Chem. Int. Ed.*, 2010, **49**, 441-444.
33. W. Ho, Z. Zhang, W. Lin, S. Huang, X. Zhang, X. Wang and Y. Huang, *ACS Appl. Mater. Interfaces*, 2015, **7**, 5497-5505.
34. M. K. Bhunia, K. Yamauchi and K. Takanabe, *Angew. Chem.*, 2014, **126**, 11181-11185.
35. G. Kresse and J. Furthmüller, *Comput. Mater. Sci.*, 1996, **6**, 15-50.
36. J. P. Perdew, K. Burke and M. Ernzerhof, *Phys. Rev. Lett.*, 1996, **77**, 3865-3868.
37. S. Grimme, J. Antony, S. Ehrlich and H. Krieg, *J. Chem. Phys*, 2010, **132**, 154104.
38. P. E. Blöchl, *Phys. Rev. B*, 1994, **50**, 17953-17979.
39. G. Kresse and D. Joubert, *Phys. Rev. B*, 1999, **59**, 1758-1775.
40. F. Goettmann, A. Fischer, M. Antonietti and A. Thomas, *Angew. Chem. Int. Ed.*, 2006, **45**, 4467-4471.
41. B. V. Lotsch, M. Döblinger, J. Sehnert, L. Seyfarth, J. Senker, O. Oeckler and W. Schnick, *Chem. Eur. J.*, 2007, **13**, 4969-4980.
42. M. K. Bhunia, S. Melissen, M. R. Parida, P. Sarawade, J.-M. Basset, D. H. Anjum, O. F. Mohammed, P. Sautet, T. Le Bahers and K. Takanabe, *Chem. Mater.*, 2015, **27**, 8237-8247.
43. Q.-F. Deng, L. Liu, X.-Z. Lin, G. Du, Y. Liu and Z.-Y. Yuan, *Chem. Eng. J.*, 2012, **203**, 63-70.
44. A. Thomas, A. Fischer, F. Goettmann, M. Antonietti, J.-O. Müller, R. Schlögl and J. M. Carlsson, *J. Mater. Chem.*, 2008, **18**, 4893-4908.
45. C. Fettkenhauer, G. Clavel, K. Kailasam, M. Antonietti and D. Dontsova, *Green Chem.*, 2015, **17**, 3350-3361.
46. Q. Li, J. Yang, D. Feng, Z. Wu, Q. Wu, S. S. Park, C.-S. Ha and D. Zhao, *Nano Res.*, 2010, **3**, 632-642.
47. L. S. Kibis, A. I. Stadnichenko, S. V. Koscheev, V. I. Zaikovskii and A. I. Boronin, *J. Phys. Chem. C*, 2012, **116**, 19342-19348.
48. S.-W. Bian, Z. Ma and W.-G. Song, *J. Phys. Chem. C*, 2009, **113**, 8668-8672.